Supplementary Material

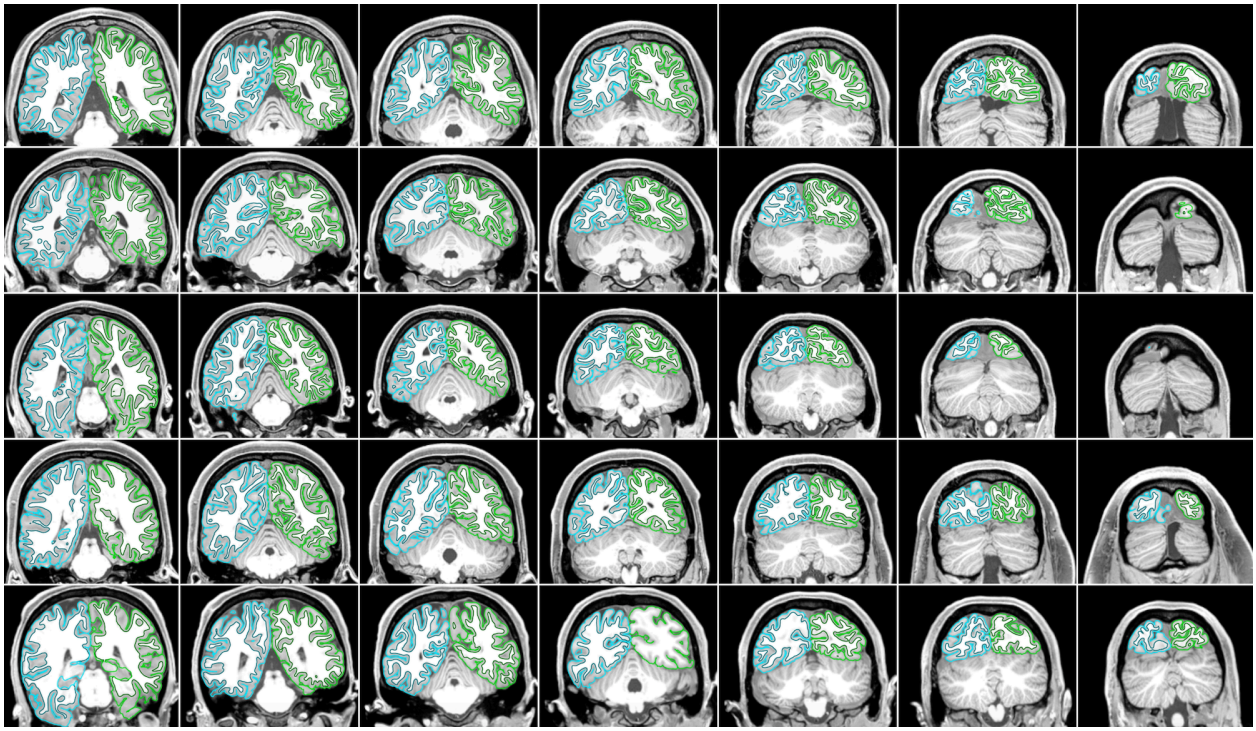

Supplementary Movie 1. Inspection of pre-processing results. Movie available online (https://osf.io/s5kw7/). Each row corresponds to a distinct subject (S1–S5), and each column corresponds to a distinct slice of the GE-EPI acquisition (every 10th slice is shown, yielding a slice-to-slice distance of 0.8 mm × 10 slices = 8 mm). The movie cycles between the mean EPI volume, the T_2-weighted anatomical volume, and the T_1-weighted anatomical volume. For each volume, contours depicting the white-matter and pial surfaces are toggled on and off (green and cyan indicate left and right hemispheres, respectively). The results demonstrate that EPI undistortion, co-registration between functional and anatomical volumes, and cortical surface reconstruction all performed well.

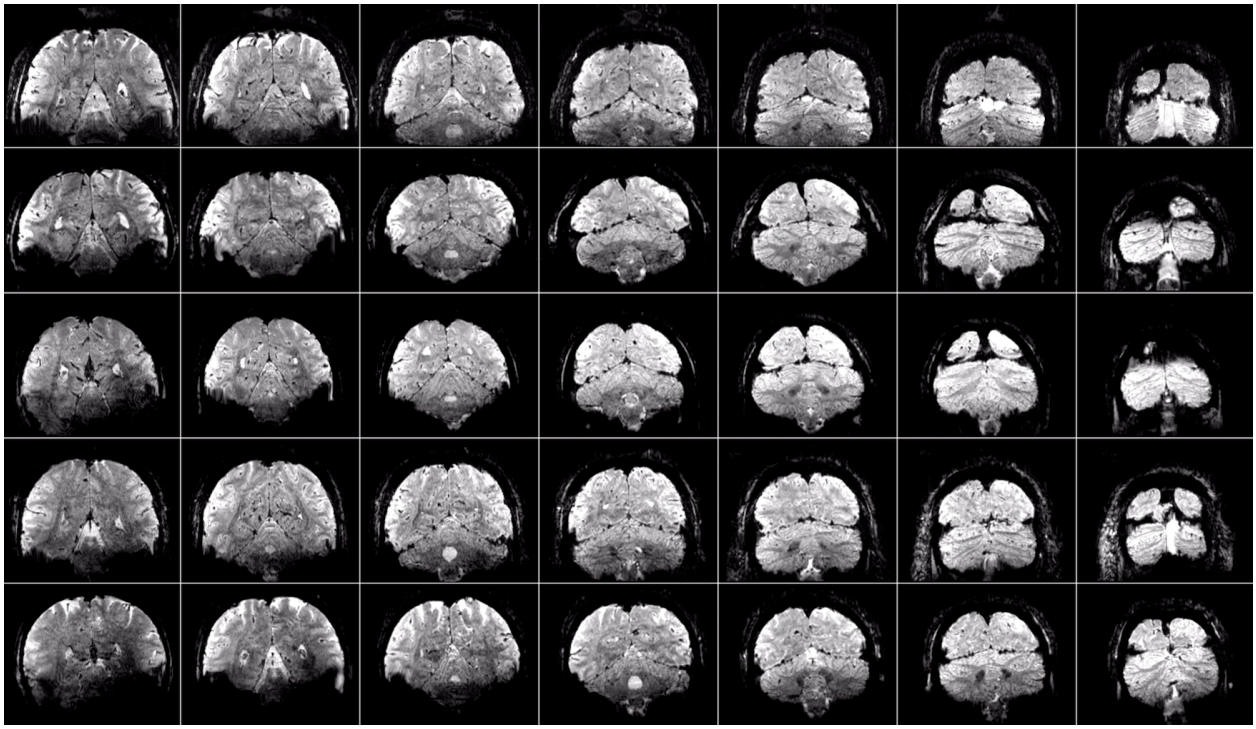

Supplementary Movies 2–4. Functional volumes after pre-processing. Movies available online (https://osf.io/s26yz/, https://osf.io/jbpv5/, https://osf.io/axfvt/). Row and column format same as **Supplementary Movie 1**. These movies show a sequence of 50 EPI volumes chosen randomly from all volumes acquired within a given scan session (which lasted ~80 min). The volumes are raw volumes aside from the temporal resampling and spatial resampling operations that comprised pre-processing (see Methods). Visualizing randomly chosen volumes (as opposed to volumes in chronological order) is a stringent test of data quality, as it accentuates instabilities over time. Three movies are provided: **Supplementary Movie 2** shows results using the pre-processing described in the Methods, involving time-varying fieldmap estimates (multiple-fieldmap approach); **Supplementary Movie 3** shows results using identical pre-processing procedures except that the first fieldmap acquired in each scan session is used as a static fieldmap estimate that is applied to each EPI volume before subsequent motion estimation and other processing steps (single-fieldmap approach); and **Supplementary Movie 4** shows results using identical pre-processing procedures except that no fieldmap-based undistortion is applied (no-fieldmap approach). Inspection of **Supplementary Movie 2** reveals the existence of some low spatial frequency artifacts. However, overall stability over time is high in most parts of the brain, indicating that data acquisition was stable and that motion correction and fieldmap-based EPI undistortion performed well. Inspection of **Supplementary Movies 3 and 4** indicates that temporal stability is relatively high for the multiple-fieldmap and no-fieldmap approaches but is somewhat low for the single-fieldmap approach. We speculate that this temporal instability is the result of inaccurate undistortion of EPI volumes acquired distant in time from the single fieldmap and that the use of multiple fieldmaps helps mitigate this issue.

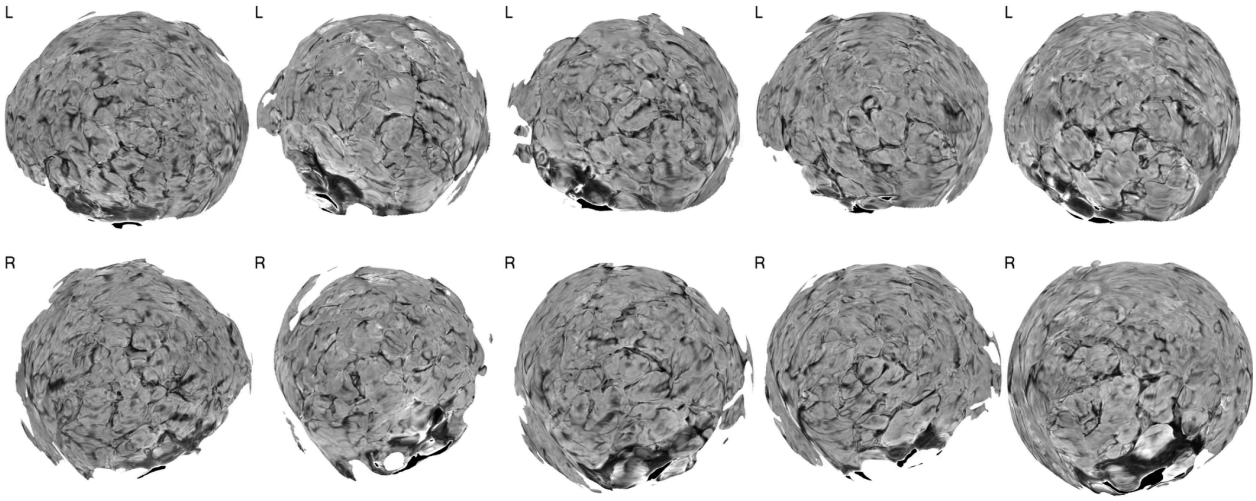

Supplementary Movie 5. Static susceptibility effects as a function of cortical depth. Movie available online (https://osf.io/2b469/). This movie shows bias-corrected EPI intensities (posterior view, spherical surface), progressing from inner to outer cortical depths (Depth 6 through Depth 1). Rows indicate left and right hemispheres; columns indicate distinct subjects (S1–S5); and the colormap for each image ranges from 0–2, as in **Figure 5** and **Figure 9B**. The large influence of cortical depth on static susceptibility effects is visible in this movie.

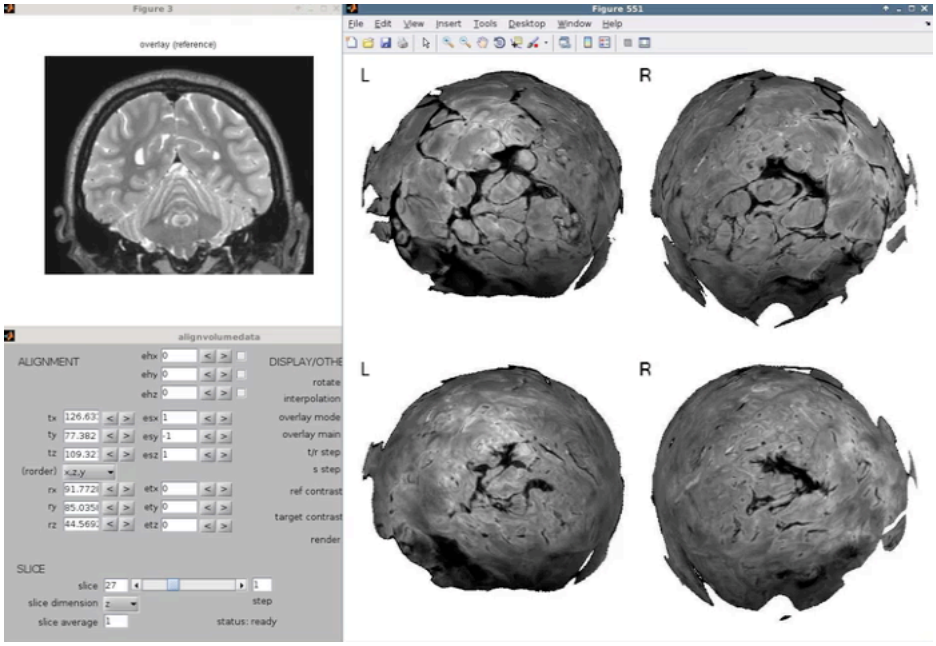

Supplementary Movie 6. Impact of registration on EPI intensities. *A*, Full movie showing registration parameters and EPI intensities. Movie available online (https://osf.io/snb2h/). This movie shows changes in registration quality and surface-mapped EPI intensities as the registration between the EPI and T_2 volumes progresses for an example subject (Subject S3). At the top left is a slice through the T_2 volume that corresponds to a specific EPI slice. At the bottom left are the registration parameters. At the right are surface visualizations of the outermost depth (Depth 1, top row) and the innermost depth (Depth 6, bottom row) (posterior view, spherical surface). The surface visualizations show raw intensities sampled from the EPI volume (cubic interpolation). At each iteration, registration parameters are updated, followed by updates to the T_2 slice (with a rapid alternation against the EPI slice to assess the match) and updates to the surface visualizations. We see that initially, the co-registration between EPI and T_2 is poor and there are large swaths of darkness in the surface visualizations. Over time, the co-registration improves and the swaths of darkness are reduced. Overall, this movie provides intuition for how imperfections in registration may lead to apparent dark intensities, and suggests that the final registration solution and its corresponding patterns of EPI intensities are robust and accurate. *B*, Movie showing only surface visualizations. Movie available online (https://osf.io/f28mc/). This movie progresses much more rapidly than the movie from panel A. We see that over the course of the optimization, large changes occur rapidly in the first several iterations and then small refinements take place until the search settles to a local minimum.

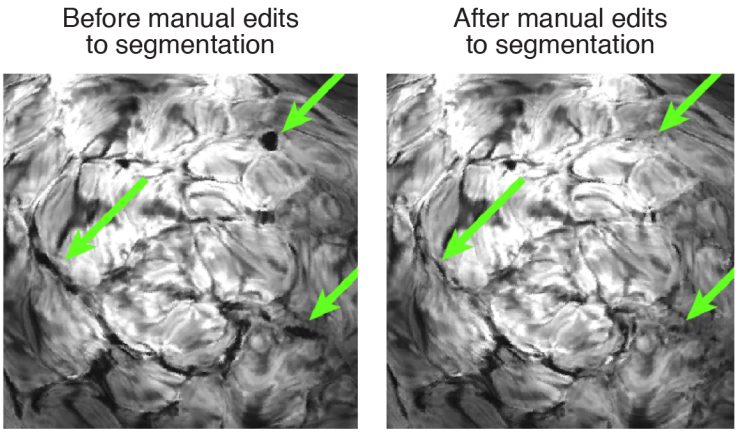

Supplementary Figure 1. Impact of manual segmentation edits. Here we plot maps of raw EPI intensities (posterior view, spherical surface, left hemisphere, Subject S1, Depth 1) generated using either the original FreeSurfer surfaces with no manual editing (left) or FreeSurfer surfaces after manual edits to the tissue segmentation (right). Green arrows highlight a few regions that undergo noticeable changes. The similarity of the two depicted maps suggests that surface errors play a limited role in shaping the EPI intensity patterns that we observe in our data.

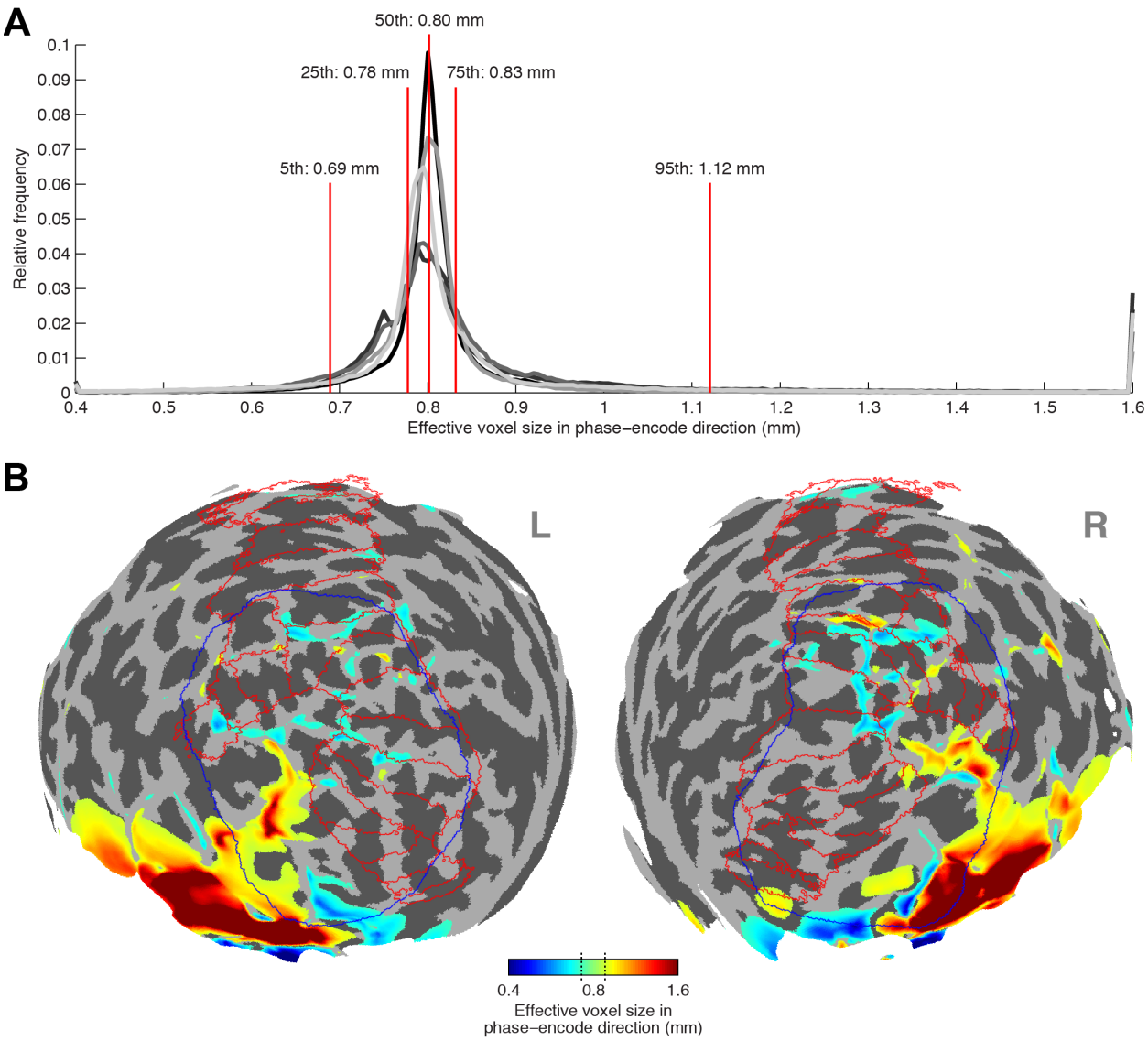

Supplementary Figure 2. Quantification of impact of EPI distortion on spatial resolution. *A*, Histogram of effective voxel sizes across all surface vertices and depths. Different shaded lines indicate different subjects, and red lines indicate percentiles calculated on results aggregated across all subjects. The results show that, for our acquisition protocol, the loss and gain in spatial resolution due to EPI distortion is, on the whole, modest: 90% of all effective voxel sizes lie within 0.69 mm to 1.12 mm. *B*, Surface visualization of effective voxel size (posterior view, spherical surface, Subject S1). Depicted is effective voxel size averaged across cortical depth. A log-based colormap is used, and we mask out values differing by less than 10% from the nominal acquisition resolution of 0.8 mm (see dotted lines). As expected, there are large distortions near the ear canals. Also, there appears to be some tendency for distortions to be located in and around gyri, perhaps due to proximity to the cerebral sinuses.

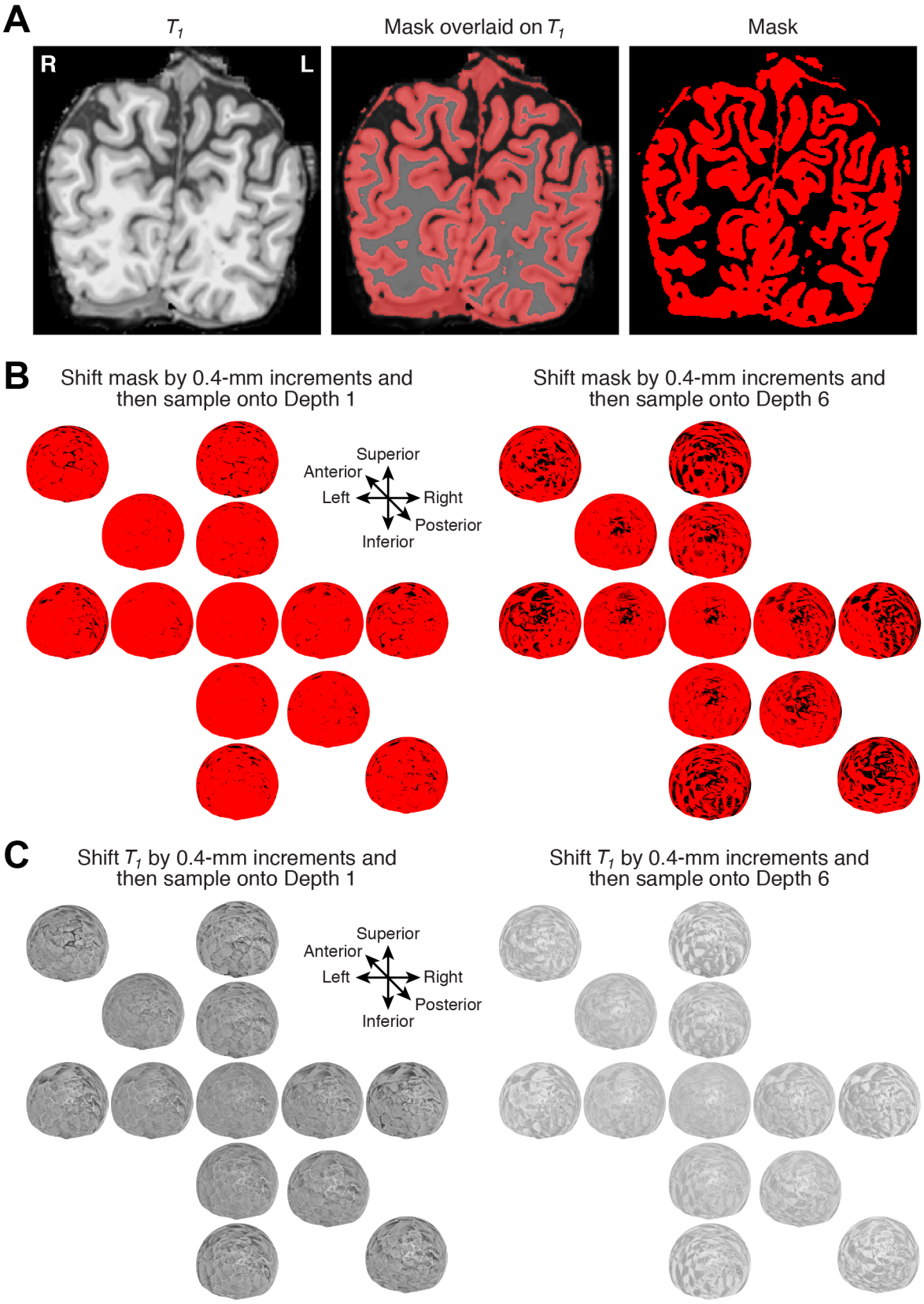
A
T_1
Mask overlaid on T_1
Mask
R
L
B
Shift mask by 0.4-mm increments and then sample onto Depth 1
Shift mask by 0.4-mm increments and then sample onto Depth 6
Superior
Anterior
Left
Right
Posterior
Inferior
C
Shift T_1 by 0.4-mm increments and then sample onto Depth 1
Shift T_1 by 0.4-mm increments and then sample onto Depth 6
Superior
Anterior
Left
Right
Posterior
Inferior

Supplementary Figure 3. Assessment of surface accuracy. It is possible that dark EPI intensities might be the result of inaccurate cortical surface reconstructions (e.g. surfaces might extend outside of the brain) as opposed to reflecting venous susceptibility effects. Though this is an issue that is difficult to definitively resolve, we perform here, for an example subject (Subject S1), a visualization to provide evidence that surface errors are likely a minor effect. The idea behind the visualization is to confirm that cortical surface vertices are located in positions that correspond to gray matter. *A*, T_1-based gray-matter mask. First, we took the *brainmask.mgz* version of the T_1 volume from FreeSurfer and upsampled the volume to isotropic 0.4-mm voxels (cubic interpolation) to reduce discretization effects. Then, we applied a simple threshold to the T_1 intensity values in order to select voxels that likely correspond to gray matter locations (values within the range 50–100). Shown is an example coronal slice through the T_1 (left), voxels in the mask (right), and an overlay of the two (middle). The mask does not perfectly isolate gray matter but is sufficient for the present purposes. *B*, Visualization of consistency between the mask and cortical surfaces. We sampled the mask using nearest-neighbor interpolation onto the Depth 1 (left) and Depth 6 (right) surfaces, and generated surface visualizations (posterior view, spherical surface, left hemisphere). Importantly, we applied various amounts of shifts to the mask before the sampling. In each set of images, the central image shows the result of no shifting, whereas the other set of 3 orthogonal dimensions x 2 directions x 2 shifts = 12 images shows results produced after shifting. The two shifts along each direction correspond to 1-voxel (0.4 mm) and 2-voxel (0.8 mm) shifts. Notice that the central image in each set of images is predominantly red, whereas small shifts of the mask lead to encroachment of black into the maps. These results provide some evidence that the cortical surfaces are positioned accurately with respect to gray matter. The dark spots in the central map of the Depth 6 results are due to unusually bright T_1 intensities found in the most posterior regions of cortex (see panel C). *C*, Visualization of consistency between the original T_1 values and cortical surfaces. Here we repeat the analysis of panel B but use the original T_1 values (no thresholding) and sample these values using cubic interpolation onto the Depth 1 and Depth 6 surfaces. A fixed colormap is used for all maps (same colormap of panel A). Compared to the binarized intensities in panel B, the visualizations in panel C are harder to interpret but are generally consistent.

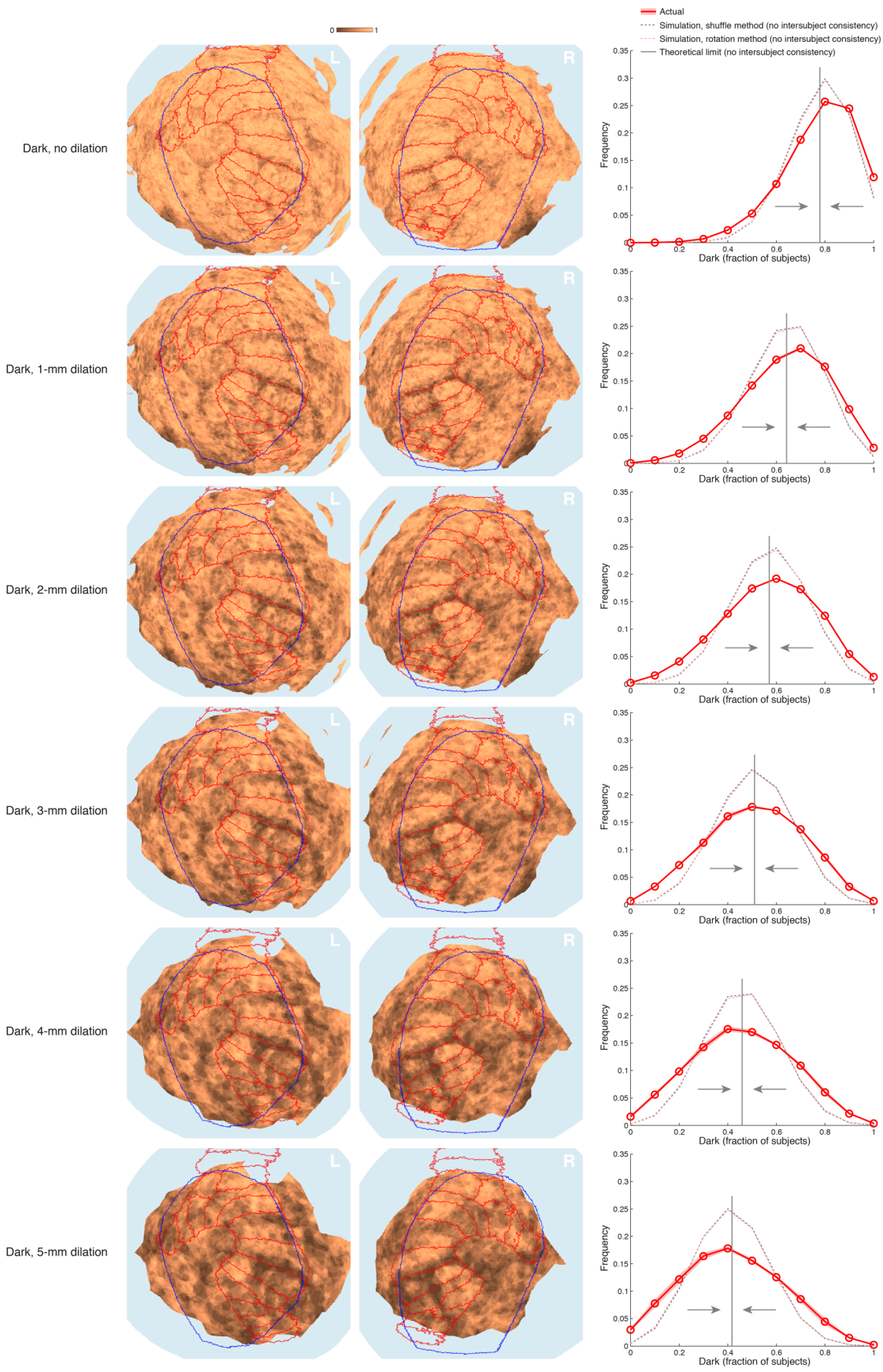
0
1
Dark, no dilation
Dark, 1-mm dilation
Dark, 2-mm dilation
Dark, 3-mm dilation
Dark, 4-mm dilation
Dark, 5-mm dilation
L
R
Actual
Simulation, shuffle method (no intersubject consistency)
Simulation, rotation method (no intersubject consistency)
Theoretical limit (no intersubject consistency)
Frequency
Dark (fraction of subjects)

Supplementary Figure 4. The effect of mask dilation on group-wise consistency of static susceptibility effects. Same format as panels B and D from **Figure 8** (except sulci lines and visual area labels are omitted for simplicity). Each row shows results obtained using different degrees of dilation: vertices in the vein masks expand to a circle with diameter *D* where *D* ranges from 0 (no dilation) to 5 mm. The main effect of increased dilation is lower values in the averaged vein mask; this is reflected in the general leftward shifts of the histograms. Independent of the specific amount of mask dilation, we see that the intersubject consistency of static susceptibility effects is greater than that observed under the null distributions.

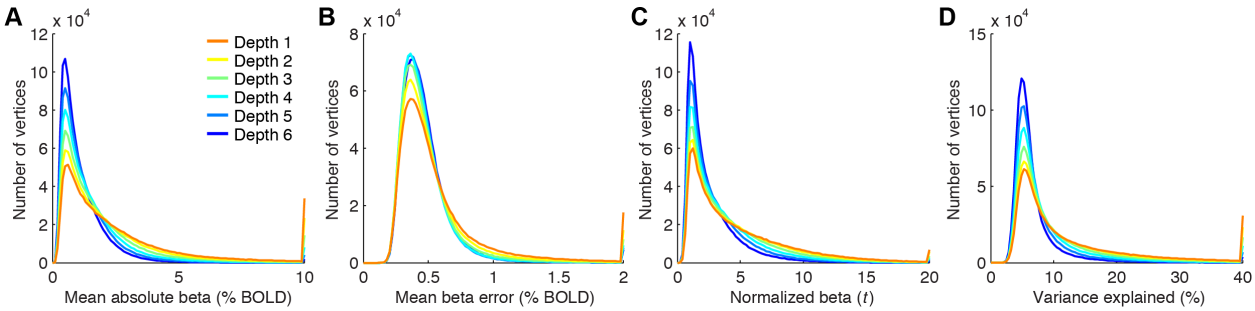

Supplementary Figure 5. Summary of GLM metrics as a function of cortical depth. Each GLM metric is aggregated across subjects and then plotted as a histogram. The rightmost bin includes all values greater than the maximum displayed value. The results indicate that outer depths are associated with large beta weights (panel A), large beta errors (panel B), large normalized betas (panel C), and large amounts of variance explained (panel D).